Incomplete approach to homoclinicity in a model with bent-slow manifold geometry

S. Rajesh[1] and G. Ananthakrishna[1,2,⋆]

[1] *Materials Research Center,*
Indian Institute of Science,
Bangalore - 560012.
India.
[2] *Center for Condensed Matter Theory,*
Indian Institute of Science,
Bangalore - 560012.
India.

Abstract: The dynamics of a model, originally proposed for a type of instability in plastic flow, has been investigated in detail. The bifurcation portrait of the system in two physically relevant parameters exhibits a rich variety of dynamical behaviour, including period bubbling and period adding or Farey sequences. The complex bifurcation sequences, characterized by Mixed Mode Oscillations, exhibit partial features of Shilnikov and Gavrilov-Shilnikov scenario. Utilizing the fact that the model has disparate time scales of dynamics, we explain the origin of the relaxation oscillations using the geometrical structure of the bent-slow manifold. Based on a local analysis, we calculate the maximum number of small amplitude oscillations, s, in the periodic orbit of L^s type, for a given value of the control parameter. This further leads to a scaling relation for the small amplitude oscillations. The incomplete approach to homoclinicity is shown to be a result of the finite rate of 'softening' of the eigen values of the saddle focus fixed point. The latter is a consequence of the physically relevant constraint of the system which translates into the occurrence of back-to-back Hopf bifurcation.

PACS number(s): 05.45.Ac, 83.50.-v, 62.20.-x

Keywords : Portevin - Le Chatelier effect, chaos, stick-slip dynamics, slow manifold, mixed mode oscillations, homoclinic bifurcation.

⋆ Electronic mail: garani@mrc.iisc.ernet.in

1 Introduction

Number of autonomous dynamical systems exhibit complex bifurcation sequences with alternate periodic-chaotic states in control parameter space. The chaotic states are usually predominant mixture of the periodic states occurring on either side of the chaotic states. These periodic states are characterized by combinations of relatively large amplitude excursions and small amplitude near harmonic oscillations of the trajectories and have been referred to as mixed mode oscillations (MMOs) in the literature. The MMOs and the accompanying complex bifurcation sequences have been observed in models and experiments in various fields of chemical kinetics [1–8], electrochemical reactions [9–12], biological systems [13], and in many other physical systems[14,15].

Both numerical as well as analytical studies have been carried out extensively to the explain the origin of the MMOs and the complex bifurcation sequences these systems exhibit[9–12,16–23]. Even though the origin of complex bifurcation sequences and the accompanying MMOs may depend on the particular system under study, almost all proposed mechanisms suggest that these bifurcation portraits are the artefact of global bifurcations of the system [17]. Investigations into the global nature of the bifurcations of the MMOs and the complex bifurcation sequences have shown that homoclinic bifurcations may be relevant to a wide variety of systems which display the MMOs. Shilnikov[24] has shown that if a dynamical system possesses a homoclinic orbit which is bi-asymptotic to a saddle focus type of equilibrium set satisfying the Shilnikov condition, then there are countably infinite number of periodic solutions in the vicinity of this homoclinic orbit. The analysis also shows that in the vicinity of this homoclinic orbit, complex bifurcation sequence can be expected in the phase portrait [17,18].

Another approach to explain the complex bifurcation sequences has been through Gavrilov - Shilnikov scenario. It has been shown that systems having homoclinic tangencies to periodic solutions possess quasi-random dynamics and MMO like behavior in the control parameter space[25]. Each of these scenarios are characterized by bifurcation diagrams obtained from the stability analysis of the homoclinic orbit and by the corresponding scaling relations involved in the approach to the homoclinicity. Apart from these studies on the homoclinic bifurcations of the continuous time systems, attempts have also been made to study the MMOs through discrete maps [19–21].

In order to understand the numerically obtained Poincare maps from such model systems and those obtained from experiments, attempts have been made to derive map structure starting from local analysis[18,22,23]. Such attempts have been reasonably successful in the sense that the features predicted by the derived maps agree with the features of the numerically obtained Poincare maps. However, due to the very nature of global bifurcations, there is no easy way of classifying the entire complex bifurcation sequences of these systems. Hence numerical evidence plays a crucial role in classifying the dynamics of these systems.

Yet another approach to the understanding of these complex bifurcation sequences and the MMOs is based on the analysis of the structure of the slow manifold [4,10,11,26–28] of the system of equations. A standard slow manifold structure that has been used in the study of MMOs is the $S-$shaped structure[29,30] wherein the upper and lower pleats are attractive and the middle branch is repulsive. By appropriately locating the fixed point on the upper or

lower pleat, the origin of MMOs has been explained[26]. In this construction of slow manifold, Shilnikov's criterion is satisfied if the direction of approach of the fast variable is transverse to the slow manifold containing the fixed point. However, in many situations[6,10,11], including the system under study, the approach to the saddle fixed point by the fast variable is not transversal. Depending on the nature of the approach of the fast variable to the fixed point, a classification for the MMOs has been suggested by Koper *et. al.* [11] as type-I and type-II corresponding to the tangential approach and transversal approach (to the slow manifold) respectively. It has also been suggested that the occurrence of MMOs and incomplete approach to homoclinicity is related to the presence of Hopf bifurcation close to the fold of the S-shaped slow manifold structure [10].

In this paper, we analyze the complex dynamical behavior of a model which has been introduced in the context of a type of plastic instability called the Portevin - Le Chatelier effect. The model exhibits a rich variety of dynamics such as period bubbling, doubling and the complex bifurcation sequences. Two distinct features of the model are the atypical nature of the relaxation oscillation and the MMOs. The latter exhibits partial features of Shilnikov, and Gavrilov-Shilnikov scenario and shows a incomplete approach to the homoclinic point. Our effort is focussed in understanding this issue in the context of our model. To begin with we study the nature and the origin of the relaxation oscillations by analyzing the geometry of the slow manifold which controls the relaxation oscillations. We show that the underlying cause of the relaxation oscillations is due to the atypical bent geometry of the slow manifold. This feature forms the basis of further analysis of the nature of the MMO sequences, and the incomplete approach to homoclinic bifurcation. The paper is organized as follows. In section II, for the sake of completeness, we start with

a brief introduction to the phenomenon followed by a description of the model. Section III contains a detailed analysis of the complex bifurcation sequences exhibited by the model in the plane of two physically interesting parameters. Section IV contains a discussion on the origin of relaxation oscillations using the geometry of the slow manifold. Using this, we explain the origin of the MMOs and derive a scaling relation involving the maximum number of periodic orbits allowed for given value of the control parameter. The analysis helps us to understand the cause of the incomplete approach to homoclinicity. We conclude the paper with discussion and conclusions in section V.

2 A Dynamical Model for Jerky Flow

Since the model is rooted in the area of plastic instability, for the sake of completeness, we start with a brief introduction to the phenomenon. The Portevin-Le Chatelier (PLC) effect is a plastic instability manifesting when specimens of metallic alloys are deformed under tensile deformation. Under normal conditions, the stress-strain curve is smooth. However, repeated yield drops occur when the material parameters are in the regime of instability. Each of the load drops is related to the formation and propagation of dislocation bands [31,32]. The PLC effect (or the jerky flow) is seen in several metallic alloys such as commercial aluminium, brass, alloys of aluminium and magnesium [31]. The phenomenon is observed only in a window of strain rates and temperature. It is generally agreed that the microscopic cause of the instability is due to the interaction of dislocations with mobile point defects. This leads to the negative strain rate characteristic of the yield stress. The basic idea was formulated by Cottrell [33] few decades ago. However, this model and its extensions do not deal with the time dependent nature intrinsic to the phenomena.

The first dynamical description was attempted Ananthakrishna and coworkers several years ago [34,35]. The basic idea of the model is that most of the generic features of the PLC effect stem from nonlinear interactions between defect populations. The model in its original form does introduce spatial dependence of specific nature. However, further analysis of the model ignores the details of spatial inhomogeneous structure. The model consists of three types of dislocations and some transformations between them. The model has proved to be very successful in that it could explain most of the experimentally observed features such as the existence of bounds on the strain rate for the PLC effect to occur, the negative strain rate sensitivity, etc.,[35,36,39]. Several aspects of the model has been investigated [40–42].

A few comments may be in order regarding the spatial aspect of the PLC effect. The nature of spatial terms that should be introduced in the description of the PLC effect has been a controversial topic[43]. However, there is some consensus that the double cross slip mechanism plays an important role in the spatial aspect. In the above model, justification for ignoring the spatial inhomogeneous structure and considering only the temporal aspects of the phenomenon is that the variables (dislocation densities) correspond to the collective degrees of freedom of the spatially extended systems. But, if one were to be interested in spatial aspects directly, we refer the reader to an improved version of the model[44]. Further work to improve the model by including the nonlocal effects of immobile density along with the cross slip term is under active investigation.

One important prediction of the model is that the phenomena should be chaotic in a certain regime of applied strain rate[37,39,45]. This prediction

has been verified by analyzing stress signals obtained from single and polycrystalline samples [44,46–49]. Further, the number of degrees of freedom required for a dynamical description of the phenomenon estimated from the analysis was found to be four or five consistent with that envisaged in the model. Moreover, since the physical system is spatially extended, this reduction to few degrees of freedom does suggest that these modes correspond to collective degrees of freedom of the participating defects. From this point of view, dealing with the temporal aspect appears to be justified. Therefore, it is natural to investigate the chaotic behavior of the model in its own right. Some preliminary results on the chaotic aspects of the model have been published earlier [37,39,45].

The model consists of mobile dislocations and immobile dislocations and another type which mimics the Cottrell's type, which are dislocations with clouds of solute atoms [35]. Let the corresponding densities be N_m, N_{im} and N_i, respectively. The rate equations for the densities of dislocations are:

$$\dot{N}_m = \theta V_m N_m - \beta N_m^2 - \beta N_m N_{im} + \gamma N_{im} - \alpha_m N_m \tag{1}$$

$$\dot{N}_{im} = \beta N_m^2 - \beta N_{im} N_m - \gamma N_{im} + \alpha_i N_i, \tag{2}$$

$$\dot{N}_i = \alpha_m N_m - \alpha_i N_i. \tag{3}$$

The overdot, here, refers to the time derivative. The first term in Eq. (1) is the rate of production of dislocations due to cross glide with a rate constant θ. V_m is the velocity of the mobile dislocations which in general depends on some power of the applied stress σ_a. The second and third term refer to annihilation or immobilization processes. The fourth term represents the remobilization of the immobile dislocations due to stress or thermal activation (see the loss term γN_{im} in Eq. 2). The last term represents the immobilization of mobile dislocations either due to solute atoms or due to other pinning centers. α_m

refers to the concentration of the solute atoms which participate in slowing down the mobile dislocations. Once a mobile dislocation starts acquiring solute atoms we regard it as a new type of dislocation, namely the Cottrell's type N_i. This process is represented as a gain term in Eq. (3). As they acquire more and more solute atoms they will slow down and eventually stop the dislocation entirely. At this point, they are considered to have transformed to N_{im}. This process has been represented by the loss term in Eq. (3) and a gain term in Eq. (2).

These equations should be dynamically coupled to the machine equations describing the rate of change of the stress developed in the sample. This is given by

$$\dot{\sigma_a} = \kappa(\dot{\epsilon_a} - B_0 N_m V_m), \tag{4}$$

where κ is the effective modulus of the system, $\dot{\epsilon}_a$ is the applied strain rate, V_m is the velocity of mobile dislocations and B_0 is the Burgers vector. These equations can be cast into a dimensionless form by using the scaled variables

$$x = N_m \left(\frac{\beta}{\gamma}\right), y = N_{im}\left(\frac{\beta}{\theta V_0}\right),$$
$$z = N_i \left(\frac{\beta\alpha_i}{\gamma\alpha_m}\right), \tau = \theta V_0 t, \text{ and } \phi = \left(\frac{\sigma_a}{\sigma_0}\right).$$

Using the power law dependence $V_m = V_0(\frac{\sigma_a}{\sigma_0})^m$, Eqs. (1-3) and (4) can be rewritten as

$$\dot{x} = \phi^m x - ax - b_0 x^2 - xy + y, \tag{5}$$
$$\dot{y} = b_0\left(b_0 x^2 - xy - y + az\right), \tag{6}$$
$$\dot{z} = c(x - z), \tag{7}$$
$$\dot{\phi} = d\left(e - \phi^m x\right), \tag{8}$$

Here $a = (\alpha_m/\theta V_0), b_0 = (\gamma/\theta V_0), c = (\alpha_i/\theta V_0)$, $\kappa = (\theta\beta\sigma_0 d/\gamma B_0)$ and $e = (\dot{\epsilon}_a\beta/B_0 V_0\gamma)$. For these set of equations there is only one steady state

which is stable. There is a range of the parameters a, b_0, c, d, m and e for which the linearized equations are unstable. In this range x, y, z and ϕ are oscillatory.

Among these physically relevant parameters, we report here the behavior of the model as a function of most important parameters namely the applied strain rate e and the velocity exponent m. We use e as the primary control parameter for the analysis. The values of other parameters are kept fixed at $a = 0.7, b_0 = 0.002, c = 0.008, d = 0.0001$ and $k = 1.0$. The present choice of parameters *does not necessarily correspond to a realistic experimental situation,* although there is a range of allowed values. As can be verified these equations exhibit a strong volume contraction in the four dimensional phase space. We note that there are widely differing time scales corresponding to a, b_0, c and d (in the decreasing order) in the dynamics of the model. For this reason, the equations are stiff and numerical integration routines were designed specifically to solve this set of equations. We have used a variable order Taylor series expansion method as the basic integration technique with coefficients being determined using a recursive algorithm. Most of the bifurcation analyses were performed using these indigenous routines. AUTO software package[50] was used exclusively for two parameter continuation of bifurcation points.

3 Summary of bifurcation exhibited the model

In an attempt to understand the complex bifurcation sequences exhibited by the model, we start with an outline of the gross features of the phase diagram in the (m, e) plane shown in Fig. 1. In our discussion, we consider m to be the unfolding parameter. For values of $m > m_d \sim 6.8$, the equilibrium fixed point of the system of equations is stable. At $m = m_d$, we have a degenerate Hopf bifurcation as a function of e. For values less than m_d, we have a back-to-back Hopf bifurcation. The periodic orbit connecting these two Hopf bifurcations is referred to as the Principal Periodic Orbit (PPO). The dynamics of the system is essentially bounded by these two Hopf bifurcations. In Fig. 1, the broken line represents the Hopf bifurcation and the dotted lines correspond to the first three successive period doubling bifurcations leading to period 2, 4 and 8 orbits. The region in between the first period two and the Hopf bifurcation line exhibits monoperiodic relaxation like oscillations.

The PPO for most of the parameter plane (m, e) is born through a subcritical Hopf bifurcation leading to relaxation like oscillations. However, the narrow region between the Hopf bifurcation line (corresponding to large values of e) and the period two regime is characterized by small amplitude nearly symmetric coplanar limit cycles. The complex bifurcation sequences, characterized by alternate periodic-chaotic sequences seen in the parameter space, are roughly indicated by the hatched region. Since the part of the hatched region extends beyond the outermost period doubling line (large values of e and small values of m), both the MMOs and the small amplitude monoperiodic limit cycle solutions coexist in this region. (See also Fig. 3.) A codimension two bifurcation point in the form of a cusp (shown as a filled diamond) at (e_c, m_c) formed by merging of the locus of two saddle node periodic orbits (represented by bold

lines) of the PPO is also displayed in Fig. 1. Apart from these bifurcations, we failed to detect any other bifurcation or equilibrium set in the phase space. We will deal with each of these regions in detail below.

Bifurcation diagrams have been obtained by plotting the maxima of any one of the variables x,y,z or ϕ as a function of the control parameters (e, m). We have mostly shown the bifurcation diagrams in the variable x. This choice enables a good visual representation of the bifurcation diagram since the maxima of the x variable is quite large compared to other variables. Based on the nature of the bifurcation sequences, the parameter space can be broadly grouped into two regions, viz. $m \geq 2.0$ and $m < 2.0$, and we will discuss the changes as a function of e fixing m at a particular value.

3.1 Region $m \geq 2.0$

We briefly summarize the results for this region. For values of $m > 2.16$, the bifurcation diagrams are characterized by an incomplete period doubling cascades followed by reverse period doubling bifurcations, displayed as nested bubbles of periodic states (see Fig. 2). As m decreases, the number of periodic bubbles nested in the structure increases as 2^n, with $n \to \infty$, culminating in chaos. Just below $m = 2.16$, the disjoint chaotic bubbles collide with each other forming an extended attractor which has been referred to as 'bubble bursting' in the literature[51]. Similar features have been observed with m as the control parameter keeping e fixed at an appropriate value. The rates of the period doubling (PD) bifurcations as well as the reverse period doubling bifurcations with respect to e and m fall close to the value of the Feigenbaum's constant for quadratic unimodal maps, namely $\delta_F = 4.66$. When the value of m reaches a critical value $m = 2.11$, a period three cycle is born through a

saddle node bifurcation and has the largest width (in e) for $m \sim 2.0$ in this regime.

3.2 Region $m < 2.0$

For $m < 2.0$, the system exhibits qualitatively different behavior compared to $m > 2.0$, in the sense that higher order MMOs emerge gradually as m is decreased. In this region, the system exhibits complex bifurcation sequences or the alternate periodic-chaotic sequences which are characteristic to this system. The stable periodic orbits in the bifurcation sequence typically exhibit MMO nature and they are labelled by L^s, where L is the number of large amplitude loops and s is the number of small amplitude loops of the periodic orbit. These MMOs are heralded by the creation of the period three ($L^s : 1^2$) region after the PD cascade to chaos in the bifurcation plot. To illustrate the nature of bifurcations in this region, we fix the unfolding parameter at $m = 1.8$ and discuss the bifurcation with respect to e.

Figure 3 shows the bifurcation sequence with alternating chaotic and periodic states along with the higher order periodic isolas (isolated bifurcation curves). The unstable periodic orbits are shown by dashed lines. In the case of isolas, we have shown only the largest amplitude isola for any given periodicity. The first instability of the PPO through a PD bifurcation opens up a period doubled orbit having a large parameter width in e. This feature persists for the entire $m_c < m < 2.0$ regime. As in the case of $m = 2.0$, a period three isola is born through a saddle node (SN) bifurcation from the chaotic attractor. In Fig. 3, stable periodic orbits are shown to be bounded between PD bifurcation (filled circle) and the SN bifurcation (filled triangle). The sequential way SN and PD bifurcations arrange themselves to form an isola can be easily

understood by considering the behavior of the Floquet eigenvalue of the periodic orbit. The period three orbit is born in a SN bifurcation accompanied by the disappearance of the first chaotic window attractor. At this value of e, Floquet eigenvalue is at $+1$ creating a pair of stable and unstable period three orbits. As e is increased, the eigenvalue of the unstable periodic orbit increases beyond $+1$ while the eigenvalue corresponding to the stable orbit keeps decreasing and crosses -1 resulting in a PD bifurcation. Due to the isola structure, further increase in e makes this eigenvalue cross back -1 thus restabilizing the period three orbit. For any further increase in e, the Floquet eigen values of the stable and unstable orbit merge again at $+1$ and vanish in another SN bifurcation to complete the isola structure. The next higher order isola is also created through a SN resulting in the disappearance of the chaotic attractor born from the destabilisation of stable period three orbit. Higher order periodic orbits (isolas) are formed in a similar way. Note that these isolas are independent of the PPO. We refer to this sequence of periodic orbits of this form as the principal period adding sequence (PPAS) or the principal Farey sequence. In the MMO notation, the PPAS can be written as $L^s : 1^n$ where $n = 2, 3, 4, ...$ As the periodicity increases, the width of the isolas in e decreases. Since the isolas are independent of the PPO, any change in the stability of the PPO has no effect on the nature of the sequence. This is evident from the bifurcation diagram where higher periodic orbits (isolas) are seen even after stability of the PPO is reestablished. The restabilisation of the PPO is through a reverse period doubling cascade from chaos. This chaotic segment formed from the reverse period doubling of the PPO expands in an interior crisis due to its collision with an unstable periodic orbit of the next higher period isola (period three in the case of $m = 1.8$). This crisis point, shown by an arrow, marks the lower boundary of the multistability region in the bifurcation diagram.

The inset of Fig. 1 shows the expanded region of interest of the phase diagram in the (m, e) plane. As can be seen, the locus of the SN bifurcations corresponding to the MMOs are distinct and higher period SN bifurcation curves cross the lower ones resulting in the period n isola extending beyond the period $(n-1)$ isola. Moreover, the region where SN bifurcation curves overlap with the region of the period doubling curves, multistability regions in the parameter space (m, e) are created. This is clearly seen in Fig. 3 where bifurcation diagram for $m = 1.8$ is shown. (See also Fig. 4.) Typically, the same mechanism as described for the case of $m = 1.8$ operates for the period adding sequences in the region $2.0 > m > m_c$, where $m_c \sim 1.1$ is the value of m at the cusp point. As m decreases from $m = 2.0$, higher number of stable periodic windows are accommodated with concomitant decrease in the width of the chaotic regimes separating the periodic windows. The arithmetically increasing periods of the orbits going from left to right form an incomplete period adding sequence with decreasing widths for higher order periodic windows. These features are shown in the bifurcation diagrams for $m = 1.8$, and $m = 1.2$ in Fig. 3 and Fig. 4 respectively.

Below m_c, the bifurcation diagram is even more interesting and rich. Here, we outline the features related to the Farey states. For the case $m = 1.0$, only three principal Farey states denoted by L^s, $s = 1, 2$ and 3 survive, as shown in Fig. 5. The well developed sub-Farey sequences are also shown in the inset of Fig. 5. The sub-Farey states created go from right to left in contrast to the principal Farey states (see Fig. 5). All these sub-Farey sequences culminate in a SN bifurcation. While in the first bifurcation of the PPO (SN bifurcation), the transition is from $1^0 \rightarrow \infty^1$, the mid region of parameter accommodates both the large amplitude and small amplitude solutions with nearly equal weights. Towards the end region of e, we find no fine structure typical of the

first two principal chaotic windows.

4 Mechanism of relaxation oscillations

One characteristic feature of the dynamics of the system is its strong relaxation nature. This is seen even in the case of the mono-periodic solutions emerging from the Hopf bifurcation for small values of e. This feature, of course persists for other regions of the (m, e) plane where the MMO type of oscillations are also seen. These two aspects are interrelated and are a result of the structure of the slow manifold as we will show. Since our system does not follow the known homoclinic scenarios, we look for a new mechanism for the MMOs based on the mechanism proposed for the relaxation oscillations.

4.1 Relaxation oscillations

Relaxation oscillations are highly nonlinear oscillations with large amplitude excursions of the fast variable. These oscillations arise as a consequence of the existence of a fast time scales compared to the time scales of other variables in the dynamics of the system. The relaxation oscillations have been an intense area of research in the context of biological rhythms[52]. The relaxation oscillations that manifest in the model under study is a type of relaxation oscillation wherein the fast variable takes on large values for a short time after which it assumes small values of the same order of magnitude as that of the slow variables. The time spent by the fast variable in the part of phase space where the amplitude of the fast variable is small is a substantial portion of the period of the orbit. It is this type of relaxation oscillation that is dominantly seen in our system, even though other types of relaxation oscillations are also seen [36] for certain other regimes of the (m, e) plane. We shall refer to this type of relaxation oscillation as pulsed type relaxation (PTR) oscillation. A typical plot of $x(t)$ is shown in inset of Fig. 6 for $e = 200.0$ and $m = 1.2$.

In the case when two disparate time scales are present in the dynamics, using multiple scale perturbative analysis, Baer and Ernaux have shown that Hopf bifurcation can lead to relaxation type of oscillations[53]. They have shown that nearly sinusoidal solutions born out of the Hopf bifurcation change over to relaxation like oscillations in a small region of the value of the control parameter. In such a case, the crossover to relaxation oscillations is confined to the slow manifold around the fixed point. As we will see, the nature of the relaxation oscillation in our model is very different from that discussed by Baer and Ernaux. Here, it suffices to say that the PTR is a result of the evolution wherein the trajectories visiting the slow manifold region around the fixed point are pushed out to another part of the slow manifold away from the fixed point where trajectories spend considerable fraction of its period.

To understand the nature of the relaxation oscillations, we first study the structure of the slow manifold (S) and the behavior of the trajectories visiting different regions of S. Consider the slow manifold given by

$$\dot{x} = g(x, y, \phi) = -b_0 x^2 + x\delta + y = 0 \tag{9}$$

with $\delta = \phi^m - y - a$. Here, the slow variables y and ϕ (and therefore δ) are regarded as parameters. Further, as we will see below, it is simpler to deal with the structure of the slow manifold in terms of the δ instead of both y and ϕ. Then, the physically allowed solution of the above equation is

$$x = \frac{\delta + \sqrt{\delta^2 + 4b_0 y}}{2b_0} \tag{10}$$

where δ can take on both positive and negative values. Noting that b_0 is small and therefore $\delta^2 \gg 4b_0 y$, two distinct cases arise corresponding to $\delta > 0$ and

$\delta < 0$ for which $x \sim \delta/b_0$ and $x \sim -y/\delta$ respectively. Further, since the slow variable ϕ and y take on values of the order of unity, the range of $\delta = \delta(y, \phi)$ is of the same order as that of ϕ and y (as is evident from Figs. 6 and 7). Thus, we see that $x \sim -y/\delta$ is small and $x \sim \delta/b_0$ is large. For values around $\delta = 0$ and positive, we get $x \sim (y/b_0)^{1/2}$.

Let S_1 denote the region of slow manifold values of x corresponding to $\delta > 0$ and S_2 the region of slowmanifold values of x for $\delta < 0$. The bent-slow manifold structure along with the two portions of the slow manifold are shown by a bold lines in the (x, δ) plane in Fig. 6. A local stability analysis for points on S_1 and S_2 shows that $\partial g/\partial x = \delta - 2b_0 x$ is negative. This implies that the rate of growth of x is damped and hence these regions, S_1 and S_2 will be referred to as attracting. In Fig. 6, we have shown a trajectory corresponding to a mono-periodic relaxation oscillation ($m = 1.2$ and $e = 200.0$) by a thin line. As can be seen, the trajectory spends most of the time on S_1 and S_2. For points below the line $2b_0 x = \delta$ ($\delta > 0$), $\partial g/\partial x > 0$ implying a positive rate of growth of the x variable and hence we call this region as repulsive or 'unstable' (shaded region of Fig. 6). We stress here that this region is not a part of the slow manifold. Even then, the trajectory starting on S_2 does continue in the direction of increasing δ beyond $\delta = 0$. Once the trajectory is in this region, it moves up rapidly in the x direction (due to the 'unstable' nature) until it reaches $x = \delta/2b_0$ line, thereafter, the trajectory quickly settles down on to the S_1 part of the slow manifold due to the fact $\partial g/\partial x$ becomes negative. As the trajectory descends on S_1 approaching S_2, we see that the trajectory deviates away from S_1. This happens when the value of x is such that $2b_0 x < \delta$, i.e., $\partial g/\partial x > 0$. Thus, points on S_1 satisfying this condition are locally unstable. (For points in this neighborhood $\delta \sim 0.2, x \sim 50$.) Thus, the trajectory makes a jump from S_1 to S_2 in a short time. This roughly explains

the origin of the relaxation oscillation in terms of the reduced variables δ and x.

The actual dynamics is in a higher dimensional space and a proper understanding will involve the analysis of the movement of the trajectory in the appropriate space. Moreover, quite unlike the standard $S-$ shaped manifold with upper and lower attracting pleats with the repulsive (unstable) branch, in our model, both branches of the bent-slow manifold are connected, and there is no repulsive branch of the slow manifold. *Thus, the mechanism of jumping of the orbit from S_2 to S_1 is not clear.* In order to understand this, consider a 3-d plot of the trajectory shown in Fig. 7. Retaining the same notation for the 3-d regions of the slow manifold as that used for the $x-\delta$ plane, regions S_1 and S_2 are shown in Fig. 7. As can be seen, the region S_2 corresponding to small values of x lies more or less on the $y-\phi$ plane and the region S_1 corresponding to large values of x is nearly normal to the $y-\phi$ plane due to the large b_0^{-1} factor. (Note that the scales of y and ϕ are the smallest for the system.) Regions S_1 and S_2 are demarcated by the 'fold curve' which lies in the $y-\phi$ plane and is given by $\delta = \phi^m - y - a = 0$. As in the case of $x-\delta$ plane, in 3-d space also, the rapidly growing nature of the trajectory seen in the approximate region below the surface of $2b_0x = \phi^m - y - a$ and lying to right of the 'fold curve' is due to $\partial g/\partial x > 0$.

The principal features of the relaxation oscillations that we need to explain are: a) very slow time scale for evolution on S_2, b) fast transition from S_2 to S_1 and c) evolution on S_1. As mentioned in the introduction, these are related to the slow - fast time scales. In order to understand this, we shall analyze Eqs. (6) and (8) by recasting them in terms of δ. In the whole analysis it would be helpful to keep in mind the range of values of x, y, z and ϕ (shown

in Figs. 6 and 7), in particular, their values as the trajectory enters and leaves S_1. Consider rewriting Eq. (6) valid on the slow manifold S in terms of δ:

$$\dot{y} = b_0(x\delta - xy + az). \tag{11}$$

The idea is to study this equation along with Eq.(8) in specific regions of the phase space to understand the general features of the flow, viz., on S_2, just outside S_2, and on S_1. The presence of the z variable in Eq. (11) poses some problems. However, it is possible to get a rough estimate of the magnitude of z and the relative changes in the values of z which is all that will be needed for our further discussions. To see this, consider Eq. (7) from which we see that z follows x. Further, Once the trajectory moves out of S_2, x changes rapidly and therefore the value of z increases (in a relatively short interval of time), reaching its maximum value, z_{max}, just before the trajectory returns to S_2. When the trajectory is on S_2, since $x \sim y/|\delta|$, from Eq. (7) we see that the value of z is slowly decreasing (with a time constant c^{-1}) starting from z_{max}, reaching its minimum value, say z_{min}, around the time when the trajectory leaves S_2. In other words, the magnitude of z is maximum when the trajectory enters S_2 and minimum when it leaves S_2. Further, we note that $x = -y/\delta \ll x_0 = z_0 \sim e/2$ and z oscillates around its equilibrium value z_0. Thus, the values of z_{max} and z_{min} are larger than the range of allowed values of y. (Note that this is also consistent with the fact that the time scale of z is larger than that for y and ϕ.)

Consider the behavior of Eq. (11) on S_2. Using the values of $x \sim y/|\delta|$, we get

$$\dot{y} = b_0 \left[-y - \frac{y^2}{|\delta|} + az \right]. \tag{12}$$

By noting that on S_2, z decreases from z_{max} to z_{min}, we see that there is a range of small values of y for which $\dot{y} > 0$ and for relatively larger values

of y, $\dot{y} < 0$. Thus, y clearly has a turning point on S_2 beyond which y decreases.

Next, consider the changes in ϕ. Using the value of $x = y/|\delta|$ on S_2 in Eq. (8), we find that e is much larger than $\phi^m y/|\delta|$, since these variables are of the order of unity. Thus, ϕ increases linearly, at a rate close to $de << 1$. Considering the fact that $\dot{x} \sim 0$ for the entire interval the trajectory is on S_2, the time scale of evolution of the trajectory is entirely controlled by the two slow time scales of y and ϕ. This roughly explains the behavior of the trajectory on S_2.

Now consider the behavior of Eq. (11) in a small region just outside $\delta = 0$. Using $x \sim (y/b_0)^{1/2}$ valid for $\delta \geq 0$, we get,

$$\dot{y} = b_0 \left[\left(\frac{y}{b_0} \right)^{1/2} (\delta - y) + az \right] \approx b_0 \left[\frac{-y^{3/2}}{b_0^{1/2}} + az \right]. \tag{13}$$

We are interested in investigating the behavior of Eq. (13), for $z = z_{max}$, appropriate as the trajectory approaches S_2 and $z = z_{min}$, appropriate as the trajectory leaves S_2. Consider the first choice ($z = z_{max}$) corresponding to the trajectory as it approaching S_2 from outside ($\delta > 0$). Then, using the value of b_0, an order of magnitude calculation shows that there is a range of small values of y for which $\dot{y} > 0$. This implies that y grows for small y, meaning that the trajectory moves towards S_2. Now consider using $z = z_{min}$ corresponding to the situation when trajectory has left S_2. Similar estimation shows that there is a range of (relatively larger) values of y for which $\dot{y} < 0$. This implies that y decreases for relatively large values of y, meaning that the trajectory is moving away from S_2. (Note that for this case, there may or may not be a range of y for which $\dot{y} > 0$.) Thus, in both cases the directions of growth of y for small and large y just outside S_2 are consistent with the behavior of y

just inside S_2. (See Fig. 7.)

Now, consider Eq. (8) with $x \sim (y/b_0)^{1/2}$ valid for the region δ positive but small. Then,

$$\dot{\phi} = d\left[e - \phi^m \left(\frac{y}{b_0}\right)^{1/2}\right]. \tag{14}$$

Keeping in mind the order of magnitude of b_0, and the fact that y and ϕ are of the order of unity, the magnitude of $\phi^m (y/b_0)^{1/2}$ is seen to be larger than its value on S_2. Note that a quick order of magnitude calculation shows that there are values of y and ϕ such that $\phi^m (y/b_0)^{1/2}$ is of the order of e which implies that ϕ is about to decrease and therefore is near its maximum. Moreover, if anything, $\phi^m x$ in Eq. (8) increases as the trajectory tends to moves out of S_2, since $\dot{x} \sim x\delta$ just outside S_2. This implies ϕ will eventually decrease.

Combining the results on $\dot{y}$ and $\dot{\phi}$ for regions just outside and inside the 'fold', we see that the trajectory enters S_2 in the region corresponding to small values of y and ϕ, and makes an exit for relatively larger values of ϕ and y (compared to their values as the trajectory enters S_2). Finally, we can see that just to the right of $\delta = 0$ line, $\dot{x} \sim x\delta$, with δ very small, which suggests that the time constant is small. Thus, the growth of x is slow in the neighborhood of $\delta = 0$, and is tangential to the S_2 plane even in the 'unstable' region. However, once the trajectory moves away from $\delta = 0$, the growth of the trajectory is controlled by $\partial g/\partial x$ and hence the time scale of growth of x is of the order of δ^{-1} which is of the order of unity. This essentially explains why the trajectory tends to move into the 'unstable' region and grows rapidly.

Once in the 'unstable' region, the value of x continues to grow in this region

of the phase space as can be seen from Eq. (8) until the value of x is such that $\phi^m x = e$ is satisfied. Beyond this value of ϕ, $\dot{\phi}$ is negative. Thus, the trajectory leaving S_2 eventually falls onto the S_1 part of the slow manifold. We can again evaluate $\dot{y}$ and $\dot{\phi}$ just as the trajectory reaches S_1. Using $x \sim \delta/b_0$ in Eq. (11), we find

$$\dot{y} = b_0 \left[\frac{\delta}{b_0}(\delta - y) + az \right], \tag{15}$$

The sign of $\dot{y}$ is determined by the factor $(\delta - y)$ at the point where the trajectory reaches S_1. To see the relative magnitudes of δ and y, consider obtaining an equation for δ starting from $g(x, y, \delta) = 0$. Differentiating this and using $\dot{x} = 0$ on for the slow manifold, we get

$$\dot{\delta} = -\frac{b_0}{x} \left[x(\delta - y) + az \right]. \tag{16}$$

Using $x \sim \delta/b_0$ on S_1, we see that y is a fast variable compared to δ. Thus, in this interval of time, we could take $\dot{y} = 0$, i.e.,

$$\delta = y - \left(\frac{b_0 az}{\delta} \right). \tag{17}$$

Since all these variables δ, y and z are positive on S_1, we see that $y > \delta$. (Note the factor $b_0 az/\delta$ is small.) Using this in Eq. (15) we see that y decreases. Now, consider the equation for ϕ. Using $x \sim \delta/b_0$ on S_1, we get

$$\dot{\phi} = d \left[e - \frac{\phi^m \delta}{b_0} \right]. \tag{18}$$

Noting the value of b_0, we see that $\dot{\phi}$ will be negative when the trajectory reaches S_1. The time scale of evolution of y in Eq. (15) is of the order of unity while that of ϕ is $\sim d/b_0$. These time scales are relatively fast. (These statements are true only as the trajectory hits S_1.) Moreover, since x is a

fast variable, the changes in x component dominates the descent of the trajectory. Finally, as the trajectory approaches S_2, $\partial g/\partial x$ becomes positive and the trajectory jumps from S_1 to S_2. Combining these results, we see that the trajectory moves towards the region of smaller values of y and ϕ entering S_2 in a region of small values of y and ϕ.

In summary, the sequential way the orbit visits various parts of the phase space is as follows. The trajectory enters S_2 part of the slow manifold in regions of small y and ϕ making an exit along S_2 for relatively large ϕ and y. Thereafter, the trajectory moves through the 'unstable' part of the phase space before falling onto the S_1 and quickly descends on S_1. This completes the cyclic movement of the trajectory and explains the geometrical feature of the trajectory shuttling between these two parts of the manifold and the associated time scales.

Now, the question that remains to be answered is − do the trajectories always visit both S_1 and S_2 or is there a possibility that the trajectory remains confined to S_1 ? It is clear that if the former is true, relaxation oscillations with large amplitude will occur and if the latter is true, the oscillations are likely to be of small amplitude. Here, we recall that the coordinates of the saddle focus fixed point are $x_0 = z_0 \sim e/2$ which is much larger than the values of x on S_2 ($\sim y/|\delta|$). Thus, the fixed point located on the S_1 will be close to the 'fold' at the first Hopf bifurcation, $e = e_f$, since the latter occurs at small values of e ($e_f \sim 5$). Due to the unstable nature of the fixed point, the trajectories spiralling out are forced onto the S_2 part of the manifold resulting in relaxation oscillation. This point has been illustrated by considering the example of a period eleven orbit for $m = 1.2$ and $e = 267.0$ shown in Fig. 8. As is clear

from this diagram, the small amplitude oscillations are located on the S_1. As the small amplitude oscillations grow, the relaxation nature does not manifest until the orbit crosses over to S_2. To the best of the authors knowledge, the mechanism suggested here for pulsed type relaxation oscillations is new.

The above feature of the trajectories continuing in the same direction of the slow manifold (S_2) well into the 'unstable' part of the phase space is somewhat similar to *canard solutions* where the trajectories tend to follow the slow manifold well into the repulsive part of the slow manifold before jumping to a attracting branch [8,54]. The differences, however, are clear. While in canard solutions, the trajectory tends to move along the repulsive part of the slow manifold before jumping to the attracting branch of the slow manifold, in our case, the trajectory leaves the slow manifold and moves into the 'unstable' part of the phase space which is not a part of the slow manifold.

4.2 Mixed Mode Oscillations

We now consider the origin of the MMO sequences in our model. Global bifurcation scenarios are known to be relevant to the MMOs and in the introduction, we briefly mentioned two of the possible global bifurcation scenarios which display MMO like sequences. These scenarios are based on the homoclinic contacts of an equilibrium set like the saddle focus fixed point and saddle periodic orbit for the Shilnikov and Gavrilov-Shilnikov scenarios respectively. Each of these scenarios are characterized by the bifurcation diagrams obtained from the stability analysis of the homoclinic orbits and by the corresponding scaling relations involved in the approach to homoclinicity [17,23].

First, we consider the similarities of the behavior of our model with the char-

acteristic features of the Shilnikov scenario. In three dimension, the Shilnikov criterion is stated in terms of the two possible combinations of the dimensions for the invariant manifolds of the saddle-focus; the unstable manifold is two dimensional and stable manifold is one dimensional and vice versa. For these two cases, the presence of an homoclinic orbit is given by the condition $|\rho/\lambda| < 1$, where the eigen values of the fixed point are given by $\rho \pm i\omega, -\lambda$, where $\rho > 0, \lambda > 0$ for the first case and $\rho < 0, \lambda < 0$ for the latter. The analysis of the Shilnikov scenario shows that in the neighborhood of the homoclinic point, the parameter space is organized such that the period of the principal periodic orbit tends to infinity as the parameter approaches the value corresponding to the homoclinic point. In our case, the system is four dimensional, with the unstable manifold of the fixed point characterized by a pair of complex eigenvalues $\rho \pm i\omega$ ($\rho > 0$) and the stable manifold by two eigenvalues $\lambda_1 < 0$ and $\lambda_2 < 0$. Here, λ_1 stays close to zero and λ_2 is substantially negative. Thus, in our case, the criterion $|\rho/\lambda| < 1$ refers to $|\rho/\lambda_1| < 1$. We find that this condition is satisfied only in a small region just prior to the disappearance of the PPO in a Hopf bifurcation. A typical plot of the eigenvalues for $m = 1.2$ is shown in Fig. 9, where we have also shown the phase ω. Even though $|\rho/\lambda| < 1$ is not satisfied over large portion of e and m, we do see that the period of the periodic orbits tend to increase as e is increased ($m < 2.0$) which is typical of the Shilnikov scenario. A plot showing the period (of the superstable orbits) verses the deviation from estimated homoclinic point(e^*) is displayed in Fig. 10 for $m = 1.4$. (We have plotted points from period three onwards.) Here, we have taken the value of e^* to be the value of e for the onset of the last observed periodic orbit with period 12 ($e = 247.63$). It must be stated that we do not face any difficulty in locating any of the periodic orbits upto the period 12. However, *we are unable to detect the next period which we interpret as an incomplete approach* to the true homoclinic point. Here, it must be mentioned that incomplete approach to homoclinicity is quite com-

mon[2–4,6,8,10,11,13,27]. We stress that even in the region where Shilnikov criterion is obeyed, we do not observe homoclinic orbit.

One other feature which is usually seen in the Shilnikov scenario is that the reinjection of the trajectory in to the neighborhood of the fixed point is along the direction of the fast variable after which the trajectories tend to stay around the saddle focus fixed point. In our model, since x is the fastest variable, it also acts as a reinjection direction. However, a closer examination shows that the spiraling in of the orbit towards the fixed point is along the z direction which is the next fastest variable. This is evident in Fig. 11 where a typical trajectory is shown. Even more dominant feature of the Shilnikov scenario is that the successive bifurcations should be connected by the PPO. This, however, is not true in our case as we have seen earlier, since the isolas which form the period adding sequence are distinct from the PPO. This feature is clear from Fig. 3 for $m = 1.8$. In fact, this feature of the isolas being distinct from the PPO is more like that of the Gavrilov-Shilnikov scenario which requires the presence of an unstable periodic orbit *which we failed to detect* in the entire parameter region wherein nontrivial dynamics is present. This rules out the possible presence of any homoclinic bifurcation due to the saddle periodic orbit. Thus, we see that our model has partial features of both these scenarios.

The above discussion suggests that the origin of the MMOs in our model is likely to be different from the two scenarios. In order to understand the mechanism of the MMOs in our model, we will use the information on the nature of the relaxation oscillations. We first note that the fixed point (x_0, y_0, z_0, ϕ_0) is on the S_1 part of the slow manifold and moves up on S_1 as e is increased.

Both x_0 and z_0 have a near linear dependence on e namely $x_0 = z_0 \sim \frac{e}{2}$, while y_0 and ϕ_0 are practically constant. Since the fixed point is unstable, any orbit in its neighborhood will locally expand along its unstable directions. Thus, we expect to get insight into the mechanism of the MMOs by studying the rate of expansion of such orbits. In order to understand the mechanism operating in our model, let us consider a periodic orbit of $L^s : 1^{10}$ type shown in Fig. 12. If the orbit has reached the neighborhood of the fixed point, any orbit on S_1 should spiral out with a local dynamics determined by the linearized eigenvalues around the fixed point. Within this approximation, the orbit expands at rate $exp[2\pi\rho/\omega]$ per rotation around the fixed point. Assuming a linearized behavior for n rotations (for fixed values of e and m), we get

$$r_n/r_1 = \exp[2\pi(\rho/\omega)(n-1)] \tag{19}$$

where r_n is the distance measured from the fixed point after n rotations along a fixed direction in the unstable manifold of the fixed point. Here, r_1 is the value of r_n for $n = 1$. Since Eq. (19) is based on linearized approximation, the values of r_n obtained from the phase plots will be in general different due to the influence of nonlinearities. For this reason, we will first study the region of validity of Eq. (19). We note that the unstable manifold is nearly in $x - z$ plane and in the neighborhood of the fixed point, the major contribution to r_n comes from x and z. Thus, it would be sufficient to consider $x(t)$ (or $z(t)$) in place of r_n and in particular, we will use the minima or maxima to analyze the small amplitude oscillations of the periodic orbit using Eq. (19). Consider the plot shown in Fig. 12. We note that the time interval between the successive minima or maxima of $x(t)$ can be taken to correspond to one rotation of the orbit. We shall denote the the deviations of the n-th minimum from the fixed point value, $x_0(e) - x_n^{min}$, by x_n^*. In Fig.12, $x(t)$ and $z(t)$ are plotted along with their fixed point values ($x_0 = z_0 = 137.82$). (We have also shown regions of

$x(t)$ corresponding to regions S_1 and S_2 of the slow manifold.) The decreasing nature of the maxima values of the amplitude of $x(t)$ for the first few cycles is a reflection of the fact that the orbit has not reached the neighborhood of the unstable manifold of fixed point lying on S_1 (see Fig. 11). It is only later (in time) that the expanding nature of the oscillations manifest, seen as the increase in the magnitude of the successive maxima values of $x(t)$. Thus, the value of x_1^* read off from $x(t)$ (in place of r_1) will contain contributions arising from reinjection mechanism. Hence, identifying x_1^* as representing the value of the first minimum of $x(t)$ would be an incorrect, if one wishes to use Eq. (19). Thus, x_1^* has to be estimated by extrapolating the values of x_n^* using values of n where nonlinearity plays an insignificant role, *i.e.*, $n > 3$ for the case of Fig.12. We denote this extrapolated value by $x_1^\dagger$. In addition, as the amplitude grows as a function of n, one should also expect that the linear dynamics breaks down. Thus, for larger n values, we should again see the effect of nonlinearity. In fact, this feature shows up as a decrease (though marginal) in the time interval between successive minima for higher n as can be verified from Fig. 12 (seen between the ninth and the tenth peaks).

Now, we attempt to estimate the *changes* in the magnitude of the small amplitude oscillations located on S_1 as a function of e and estimate at what value of e the trajectory hits the 'fold' between S_1 and S_2. We denote the distance of the fixed point $(x_0(e), y_0(e), z_0(e), \phi_0(e))$ from the 'fold' given by $D = ((x_0(e)-x_0(e_f))^2+(y_0(e)-y_0(e_f))^2+(z_0(e)-z_0(e_f))^2+(\phi_0(e)-\phi_0(e_f))^2)^{\frac{1}{2}}$, where $(x_0(e_f), y_0(e_f), z_0(e_f), \phi_0(e_f))$ refers to the value of the fixed point at the first Hopf bifurcation ($e = e_f$). Further, we note that the fixed point is close to the 'fold' at the first Hopf bifurcation and noting $x_0 = z_0 \sim \frac{e}{2}$ with a very weak dependence of y_0 and ϕ_0 on e. Thus, in one dimension where we are dealing with x variable alone, we can take $D \sim x_0(e) - x_0(e_f)$. (Note that position of

'fold' is insensitive to e.) Using the fact that $x_0(e_f)$ is small, we get $D \sim x_0(e)$. Using this, we will attempt to find the maximum value of n allowed for which the condition $x_n^* > D$ is satisfied. For this, we need to know the dependence of ρ and ω on e which decides the rate of growth of the small amplitude oscillations as a function of e. In the range of the MMO sequences that we are interested, ρ decreases and ω increases nearly linearly as can be seen from Fig. 9. Thus, we take $\rho = \rho_0 - m_\rho e$ and $\omega = \omega_0 + m_\omega e$, where, m_ρ and m_ω are the corresponding slopes. These are evaluated numerically as the best fit for the region of interest of e. The fit yields $\rho_0 = 0.10433, m_\rho = 0.0003632, \omega_0 \approx 0$ and $m_\omega = 0.0004114$ for the case shown in Fig. 12. Using this in Eq. (19) gives

$$\frac{x_n^*}{x_1^*} = \exp[2\pi(\rho/\omega)(n-1)] = \exp\{[k_1 + k_2/e](n-1)\} \tag{20}$$

Here k_1 and k_2 are functions of ρ_0, m_ω and m_ρ. This equation can be interpreted as a scaling form for the small amplitude oscillations of stable periodic orbits (i.e., for a fixed n) as a function of e. Now, consider the set of all stable periodic orbits of the form L^s for a given value of m. Then, for each of these L^s orbits, the values of n ranges upto s. Since the magnitude of small amplitude oscillations of these periodic orbits depends e, we can plot $ln\, x_n^*$ versus $1/e$, where we have used x_n^* values corresponding to the n-th minimum of a periodic orbit. The plots of $ln\, x_n^*$ as a function of e^{-1} for $n = 4$ to 7 are shown in Fig. 13. In the figure, the lowest curve (+) corresponds to $n = 2$ and other successive higher curves refer to $n = 3$ upwards. The lowest band within the $n = 2$ curve corresponds to a periodic orbit of the form L^{10} and successive bands have decreasing s values. (The gaps correspond to chaotic bands between successive periodic orbits.) It is clear that the plots are linear and the slopes of the curves corresponding to $n = 4, 5, 6$ and 7 show an increasing trend, increasing in multiples of 1530 (k_2). To illustrate the presence of nonlinearity, we have also shown plots of $ln\, x_n^*$ for $n = 2$ and 3. One can

easily notice that these two curves deviate from linearity considerably for large e. In addition, we see that the slopes of these two lines are not in multiples of k_2. This suggests that it should be possible to collapse all the curves for $n > 3$ onto a single curve. Noting that the slopes of curves are in multiples of k_2, lnx_n^*/n renders them parallel and the preexponential factor which satisfies Eq.(20), denoted by $x_1^\dagger$ can be easily determined. The value of $x_1^\dagger$ so obtained can be now used in

$$\frac{x_n^*}{x_1^\dagger} = \exp[2\pi(\rho/\omega)(n-1)] \tag{21}$$

to estimate the maximum number of small amplitude oscillations allowed for any given value of e before the size of the orbit (under the linear approximation) is large enough to hit the 'fold'. This is determined by the value of $n = n_c$ at which $x_n^* = x_{n_c}^* > D \sim e/2$.

In the inset of Fig. 13, we have shown that the curves for $n = 4$ to 7 can be collapsed on to a single curve. The value of $x_1^\dagger$ obtained by extrapolating the curves $ln\,(x_n^*(e))/n$, for $n = 7$ to 4 is 5.617. We have verified that the $n = 2$ curve and to a lesser extent $n = 3$ curve deviates from the collapsed curve reflecting that nonlinearity corresponding to reinjection is dominant for these two cases. This also implies that the orbits do not approach the fixed point close enough that the linearized eigenvalues could be useful. Using the value of $\rho = 0.0073$ and $\omega = 0.1348$ for $e = 267.0$, we can now estimate the value of small period oscillations for $n = 11$ is 171.0 which is larger than $e/2$. (Here $e = 267.0$.) This means that a maximum of *nine small amplitude oscillations* are allowed *beyond the first minimum* at this value of $e = 267.0$. This is consistent with what is seen in Fig. 12. We have verified that this method of estimating the maximum number of allowed small amplitude oscillations for any given value of e works very well as long as $n > 3$ for $m = 1.2$ and

other values of m as well. For $n = 2$ and 3, the value of e at which these orbits disappear shifts to much lower values that what actually observed.

A little reflection on the above results reveal the cause of incomplete approach to the homoclinic point. Recall that the growth of small amplitude oscillations is controlled by $2\pi\rho/\omega$. We have seen that this quantity depends inversely on e. Thus, the arithmetically increasing number of small amplitude oscillations accommodated on S_1 (without the trajectory crossing over to S_2) is a direct result of 'softening' of $2\pi\rho/\omega$ as a function of e. In other words, for every small amplitude oscillation accommodated on S_1, e changes by a fixed amount commensurate with the softening rate. Thus, the number of small amplitude oscillations that can be accommodated in the allowed interval of e in the bifurcation plot will be limited. This also implies that the approach to homoclinic point can at best be asymptotic due to finite rate of softening of $2\pi\rho/\omega$, with the asymptotic nature manifesting only in the limit $k_2 \to 0$. Clearly, these results are valid under the assumption that the contribution from nonlinear terms to the growth of the small amplitude oscillations is not strong, which is substantiated by the numerical evidence that the estimated number of small amplitude oscillation allowed for a particular value of e agrees with what is numerically observed.

It may be worth pointing out here that even though the analysis given here is for MMOs of the kind 1^s, it is clear that they can be easily generalized to L^s kind of MMOs. It must be mentioned here that the 'softening' of $2\pi\rho/\omega$ is a result of the global constraint in our model, namely, the back-to-back Hopf bifurcation. Thus, we see that the apparent homoclinic scenario exhibited by the model system is completely new. We have shown that this feature coupled

with the mechanism of the relaxation oscillations operating in the model gives rise to features of MMOs common to both Shilnikov and Gavrilov-Shilnikov scenario.

4.3 Discussion and Conclusions

Some comments may be in order here about the bent-slow manifold structure of the system. The relaxation oscillations seen in this system differs qualitatively from that seen in systems with the $S-$shaped slow manifold. The major difference in the structure is that while in the $S-$ shaped manifold, there are two attractive pleats separated by a repulsive part, in our case, both pieces S_1 and S_2 of the bent-slow manifold are attractive and are connected continuously. This aspect coupled with the fact that there is no repulsive part in the bent-slow manifold as in the S- shaped manifold suggests that the mechanism causing jumps between the S_1 and S_2 is very different. The only similarity is that the number of jumps (fast transitions) accomplished by the trajectories from one part of the slow manifold (S_2) to another (S_1) and vice versa is two as in the case of $S-$shaped manifold. During the jump from S_2 to S_1, the trajectory tends to move out of the slow manifold into unstable phase space by sticking to the direction of of motion on S_2. Here the motion is accelerated due to unstable nature of the phase space. This has some similarity to *canard* type of solutions but the comparison is superficial since the unstable part of the phase space to which the trajectory moves is not a part of the slow manifold. There is another difference namely the operative time scales in the dynamics on the slow manifold. The dynamics on S_2 is slow as it is controlled by the slow variables y and ϕ, since $\dot{x} \sim 0$ for the entire interval of time the trajectory is on S_2. On the other hand, on S_1, the time dependence of a trajectory is largely controlled by the fast variable x.

We have also analyzed the effect of bent-manifold structure on mixed mode oscillations and the incomplete homoclinic scenario. We have shown that in the case of bent-manifold structure, the approach of the fast variable towards the fixed point is along the slow manifold itself eventhough the eventual approach is along the z direction. This is in direct contrast with the $S-$shaped structure where the direction of the jump of the fast variable is transverse to the slow manifold containing the fixed point as in the Rossler's $S-$shaped slow manifold. There is another possibility as pointed out by Koper *et al*[11]. In this case, the plane of relaxation oscillations is parallel to the plane of nearly harmonic small amplitude oscillations. These authors suggest that this type of dynamics may be responsible for the incomplete approach to homoclinicity since the approach to the fixed point is along the attracting pleat of the $S-$shaped manifold. However, in both cases, irrespective of the location of the fixed point, the nature of the relaxation oscillations remain the same. Moreover, in both these cases, the small amplitude oscillations(near harmonic), as well as the large amplitude (relaxation type) oscillations are well characterized. However, the nature of intermediate amplitude oscillations are not so well understood. It has been suggested in the literature that these are related to *canard* type of solutions[8,54]. The latter type of oscillations result from 'sticking' of the trajectory to the repelling part of the $S-$shaped slow manifold before jumping to the attracting pleat of the slow manifold. In our case, although the oscillations have a superficial similarity with *canard* type of solutions, it is the 'sticking' of the trajectories in the same direction of S_2 well into the unstable phase space, coupled with the fact that there is no inherent constraint relating S_1 to S_2 in the manifold structure that appears to lead to jumps of all sizes. As an illustration, we have shown a plot of the trajectory for $m = 1.8$ and $e = 190.0$ in the $x - \delta$ plane (Fig.14). It is clear

that while the small amplitude oscillations are located in the neighborhood of the fixed point, the intermediate amplitude oscillations result from the trajectory 'sticking' to the direction of the S_2 plane and moving into the 'unstable' part of the phase space by varying amounts each time the trajectory leaves S_2.

Although the bent-manifold structure is characteristic of our systems, we believe similar structure is likely to be seen in many other models and experimental systems. Particularly, in chemical kinetics where only binary collisions are permitted, models are expected to involve only quadratic or biquadratic nonlinearities. Such models are promising candidates to exhibit the bent-slow manifold structure. In experimental systems, the dominant signature to look for would be the trapping of fast variable at small values over a substantial portion of its period followed by sharply peaked pulse like behavior.

From the above discussion, we see that the bent-slow manifold structure is at the root of understanding of the pulsed type of relaxation oscillation and the MMOs. We note here that our analysis is completely local since we have used the linearized eigenvalues around the fixed point. For the same reason, the scaling relation obeyed by the small amplitude oscillations (Eq. 21 and Fig. 13) is found to be valid only where the influence of nonlinearity to the growth of these small amplitude oscillations (as a function of e) is minimal. In spite of this, the scaling relation so obtained forms the basis for estimating the maximum number of small period oscillations permitted for a given e thus explaining the origin of MMOs in the model.

Here, we mention that the relaxation oscillations arising out of the atypical bent-slow manifold structure is directly related to a dominant characteristic of

the PLC effect, namely, the negative strain rate sensitivity of the flow stress. The analysis of time scales involved in the relaxation oscillations has been useful in understanding the origin of the negative strain rate sensitivity of the flow stress which is reported elsewhere [55].

In summary, we have analyzed the dynamics of a model for a type of plastic instability due to Ananthakrishna and coworkers with particular attention to the complex dynamics exhibited by the model. We have shown that the nature of relaxation oscillations and the MMO sequences exhibited by the model is atypical. We have proposed a new mechanism for the relaxation oscillations based on the bent-slow manifold structure of the model. Using this we have explained the origin of the MMOs. We have further shown that a crucial role in organizing the dynamics is played by the physical constraint, namely, the stress oscillations are seen only in a window of strain rates. (Indeed, the model has been devised to be consistent with this experimental feature.) This constraint translates to back-to-back Hopf bifurcation in the model leading to the 'softening' of the eigenvalue of the saddle fixed point that controls the small amplitude oscillation. It is this finite rate of softening that is responsible for the incomplete approach to the homoclinic bifurcation.

5 Acknowledgements

The authors would like to thank Dr.T.M. John who was involved in the early stages of the work and one of the authors (SR) wishes to thank the theory group, Materials Research Center, IISc, for helpful discussions.

References

[1] J.C. Roux and H.L. Swinney, in : Nonequilibrium Dynamics in Chemical Systems, eds. C. Vidal and A. Pacault (Springer, Berlin, 1984).

[2] V. Petrov, S.K. Scott, and K. Showalter, J. Chem. Phys. **97** (1992) 6191.

[3] L. Györgi, R.J. Field, Z. Noszticzius, W.D. McCormick and H.L. Swinney, J. Phys. Chem. **96** (1992) 1228.

[4] A. Arneodo, F. Argoul, J. Elezgaray, and P. Richetti, Physica D **62** (1993) 134.

[5] X.J. Wang, Physica D **62** (1993) 263.

[6] M.T.M. Koper, Physica D **80** (1995) 72.

[7] I.R. Epstein and K. Showalter, J. Phys. Chem. **100** (1996) 13132.

[8] A. Milik, P. Szmolyan, H. Löffelmann, and E. Gröller, Int. J. Bifurc. Chaos **8** (1998) 505.

[9] F.N. Albahadily, J. Ringland and M. Schell, J. Chem. Phys. **90** (1989) 813.

[10] M. T. M. Koper and P. Gaspard, J. Chem. Phys. **96** (1992) 7797.

[11] M.T.M. Koper, P. Gaspard and J.H. Sluyters, J. Chem. Phys. **97** (1992) 8250.

[12] F. Argoul, J. Huth, P. Merzeau, A. Arneodo and H.L. Swinney, Physica D **62** (1993) 170.

[13] T.R. Chay, Y.S. Fan, and Y.S. Lee, Int. J. Bifurc. Chaos **5** (1995) 595.

[14] F. de Tomoasi, D. Hennequin, B. Zambon and E. Arimondo, J. Opt. Soc. Am. **B6** (1989) 45; B. Zambon, Phys. Rev. A **44** (1991) 688.

[15] S. S. E. H. Elnashaie and A. Ajbar, Chaos, Solitons & Fractals **7** (1996) 1317.

[16] J. S. Turner, J.-C.Roux, W.D. McCormick, and H.L. Swinney, Phys. Lett. A **85** (1981) 9.

[17] J. Guckenheimer and P.J. Holmes, Nonlinear oscillations, Dynamical Systems, and Bifurcations of Vector Fields (Springer, Berlin, 1990).

[18] P. Glendinning and C. Sparrow J. Stat. Phys. **35** (1984) 645.

[19] A.S. Pikovsky, Phys. Lett. A **85** (1981) 13.

[20] R.H. Simoyi, A. Wolf and H.L. Swinney, Phys. Rev. Lett. **49** (1982) 245.

[21] K. Coffman, W.D. McCormick and H.L. Swinney, Phys. Rev. Lett. **56** (1986) 999.

[22] P. Gaspard, R. Kapral and G. Nicolis, J. Stat. Phys. **35** (1984) 697.

[23] P. Gaspard and X.J. Wang, J. Stat. Phys. **48** (1987) 151.

[24] L.P. Sil'nikov, Sov. Math. Dokl. **6** (1965) 163; L.P. Sil'nikov, Math. USSR Sb. **10** (1970) 91.

[25] N.K. Gavrilov and L.P. Shilnikov, Mat. USSR Sb. **17** (1972) 467; **19** (1973) 139.

[26] D. Barkley, J. Chem. Phys. **89** (1988) 5547.

[27] M.J.B. Hauser, and L.F. Olsen, J. Chem. Soc., Faraday Trans. **92** (1996) 2857.

[28] B. Deng, Int. J. Bifurcation and Chaos **4** (1994) 823.

[29] O.E. Rössler, Z. Naturforsch. **31A** (1976) 259.

[30] J. Boissonade, J. Chim. Phys. **73** (1976) 540.

[31] B.J. Brindley and P.J. Worthington, Metall. Reviews **145** (1970) 101.

[32] L.P. Kubin, Y. Estrin and E.C. Aifantis, Organizers, *View Point Set* Scripta Metall. **29** (1993).

[33] A.H. Cottrell, Phil. Mag. **44** (1953) 829.

[34] G. Ananthakrishna and D. Sahoo, J. Phys. **D 14** (1981) 2081.

[35] G. Ananthakrishna and M.C. Valsakumar, J. Phys. **D 15** (1982) L 171.

[36] M.C. Valsakumar and G. Ananthakrishna, J. Phys. **D 16** (1983) 1055.

[37] G. Ananthakrishna and M.C. Valsakumar, Phys. Lett. A **95** (1983) 69.

[38] Non Linear Phenomena in Materials Science, Solid State Phenomena, Vols. 3-4, eds. L.P. Kubin and G. Martin (Trans Tech, Switzerland, 1988) and other references therein.

[39] G. Ananthakrishna in [38]; G. Ananthakrishna, in : Nonlinear Phenomena in Materials Science Vol. II, Solid State Phenomena, Vols. 23-24, eds. G. Martin and L.P. Kubin (Trans Tech, Switzerland, 1992).

[40] M. Bekele and G. Ananthakrishna, Phys. Rev. E **56** (1997) 6917; Int. J. Bifurc. Chaos **8** (1998) 141.

[41] M.V. Glazov, D.R. Williams and C. Laird, Appl. Phys. **A64** (1997) 373.

[42] A.J. Markworth, A. Gupta, and R.W. Rollins, Scripta Materialia **39** (1998) 481.

[43] L.P.Kubin, C. Fressengeas, and G. Ananthakrishna in : Dislocations in Solids Vol. 11, ed. F.R.N Nabarro (North-Holland, Amsterdam, 2000). (Accepted to appear)

[44] G. Ananthakrishna, Scripta Metall. **29** (1993) 1183.

[45] G. Ananthakrishna and T.M. John, in : Directions in Chaos, ed. Hao Bai-Lin (World Scientific, Singapore, 1990).

[46] G. Ananthakrishna, C. Fressengeas, M. Grosbras, J. Vergnol, C. Engelke, J. Plessing, H. Newhaeuser, E. Bouchaud, J. Planes, and L.P. Kubin, Scripta Metall. **32** (1995) 1731.

[47] G. Ananthakrishna and S. J. Noronha, in : Nonlinear Phenomena in Materials Science, Vol. III, Solid State Phenomena, Vols. 42-43, eds. G. Ananthakrishna, L.P. Kubin and G. Martin (Scitech, Switzerland, 1995).

[48] S. J. Noronha, G. Ananthakrishna, L. Quaouire, C. Fressengeas and L.P. Kubin, Int. J. Bifurc. Chaos **7** (1997) 2577.

[49] S.J. Noronha, G. Ananthakrishna, L. Quaouire and C. Fressengeas, Pramana - J. of Physics **48** (1997) 705.

[50] E. Doedal, AUTO, Software for continuation and bifurcation problems in ordinary differential equations, Department of Applied Mathematics, California Institute of Technology (1986).

[51] E. Knobloch, and N.O. Weiss, Physica D **9** (1983) 379.

[52] R. Bertram, M.J. Butte, T. Kiemel, and A. Sherman, Bull. Math. Biol. **57** (1995) 413.

[53] S.M. Baer and T. Ernaux, SIAM J. Appl. Math. **46** (1986) 721; **52** (1992) 1651.

[54] W. Eckhaus, Lect. Notes in Math. **905** (1983) 432.

[55] S. Rajesh and G. Ananthakrishna, (Communicated)

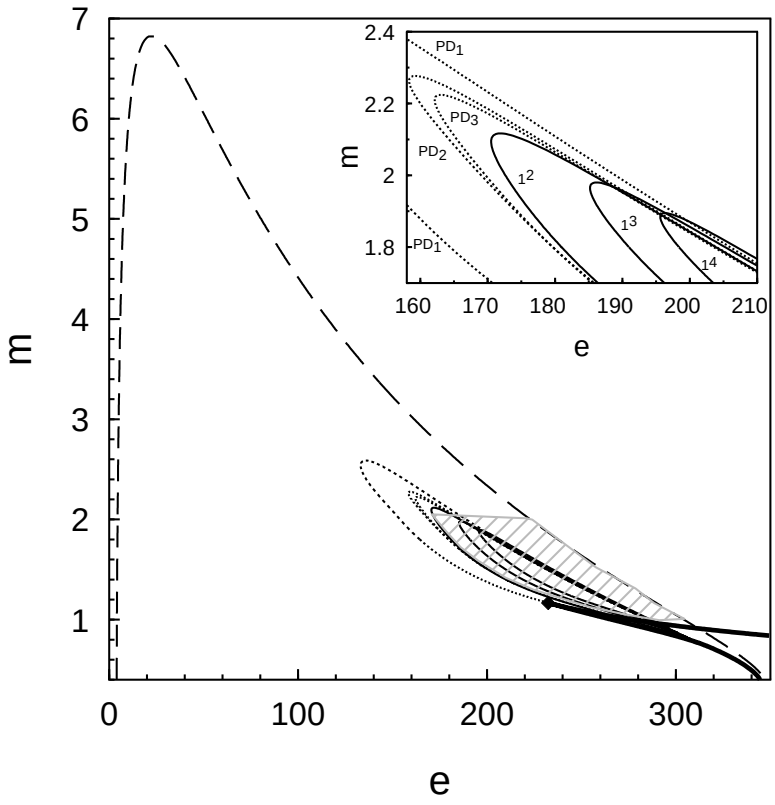

Fig. 1. Phase diagram of the model in (m, e) plane. The broken line corresponds to the locus of Hopf bifurcations, dotted lines to the PD bifurcations and the continuous lines to the locus of SN bifurcations. The thick lines represent the SN bifurcations of the PPO culminating in a codimension 2 cusp bifurcation point shown as filled diamond. Approximate region of MMOs is shown by the hatched area.

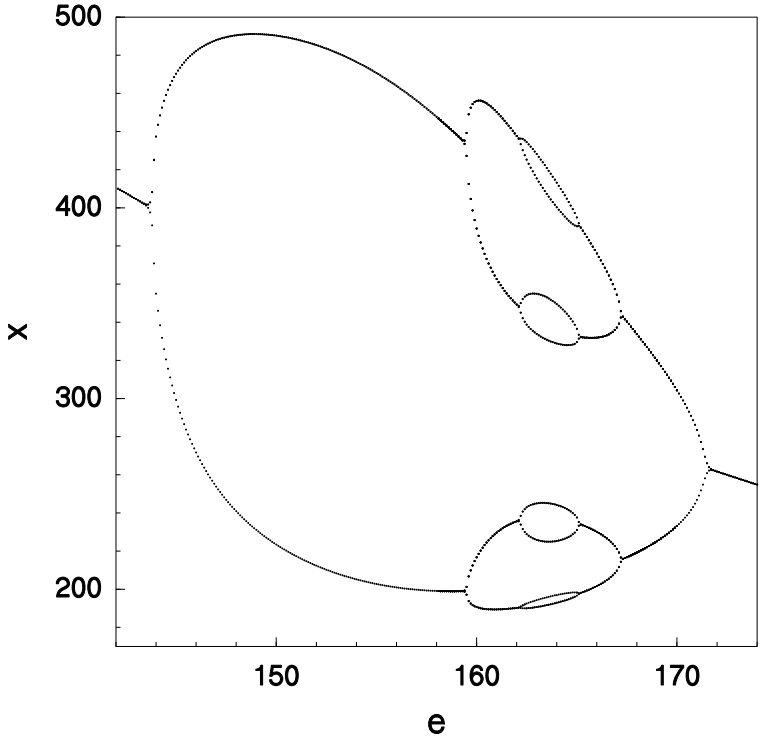

Fig. 2. Bifurcation diagram for $m = 2.215$.

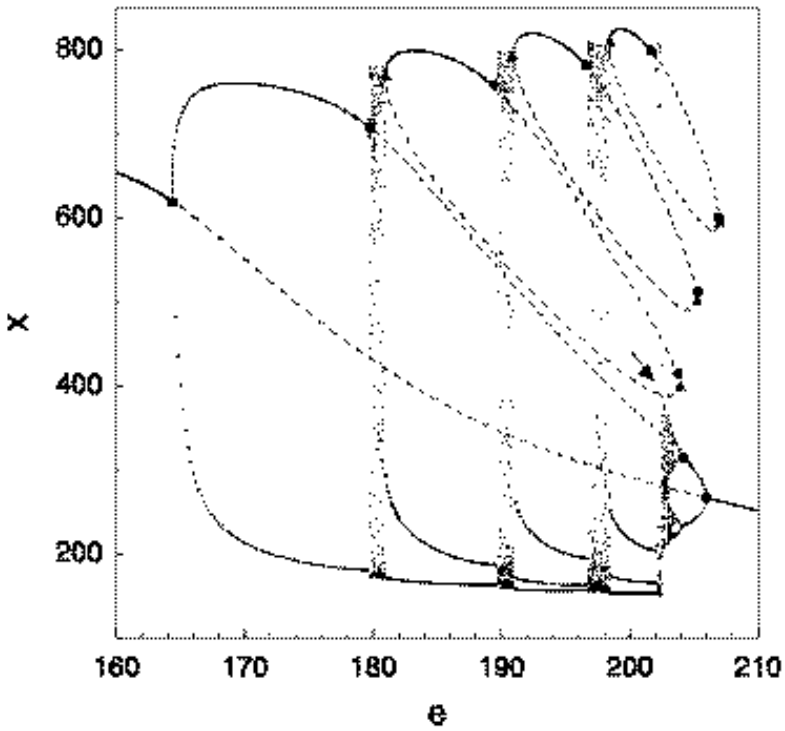

Fig. 3. The bifurcation diagram for $m = 1.8$. Dashed lines indicate unstable periodic orbits. Filled circle correspond to a PD bifurcation and filled triangle correspond to SN bifurcation. An interior crisis point is marked by an arrow.

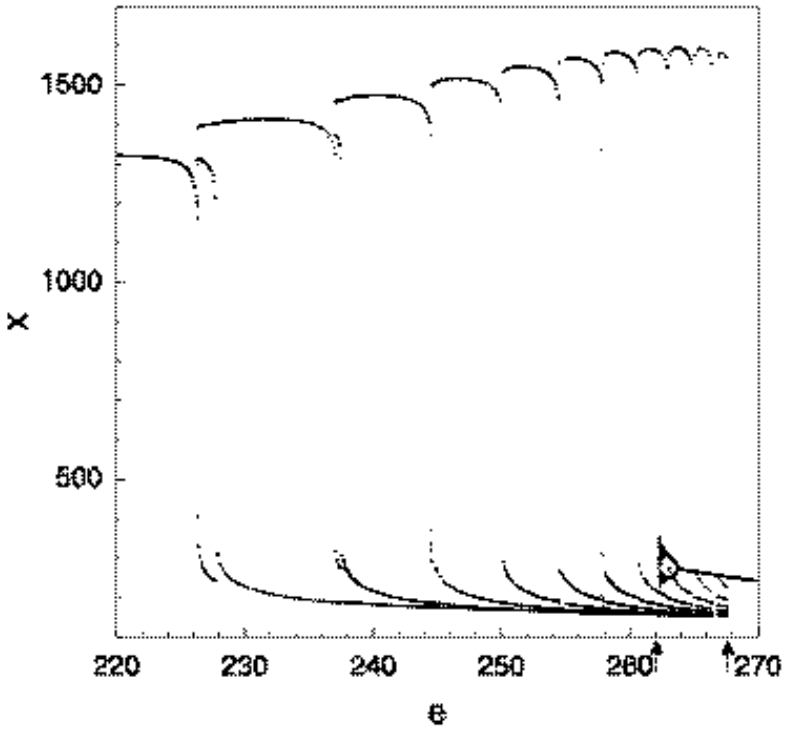

Fig. 4. Bifurcation diagrams for $m = 1.2$. The region between the arrows correspond to the coexistence region of the MMOs and small amplitude periodic orbits.

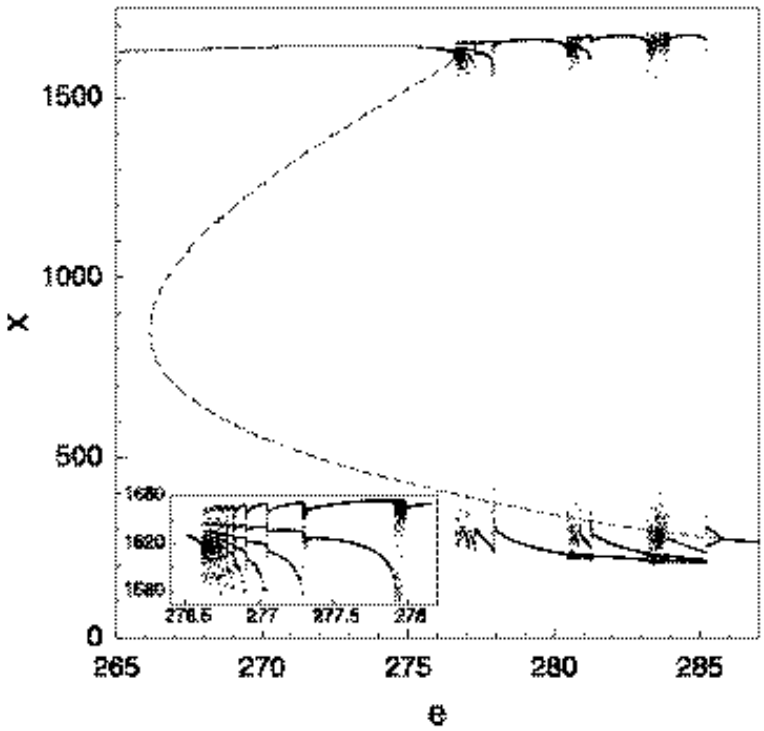

Fig. 5. Bifurcation diagram for $m = 1.0$. The dashed line indicates the unstable PPO. Inset shows enlarged portion of the bifurcation diagram where the secondary Farey sequence manifests immediately after the SN bifurcation of the PPO.

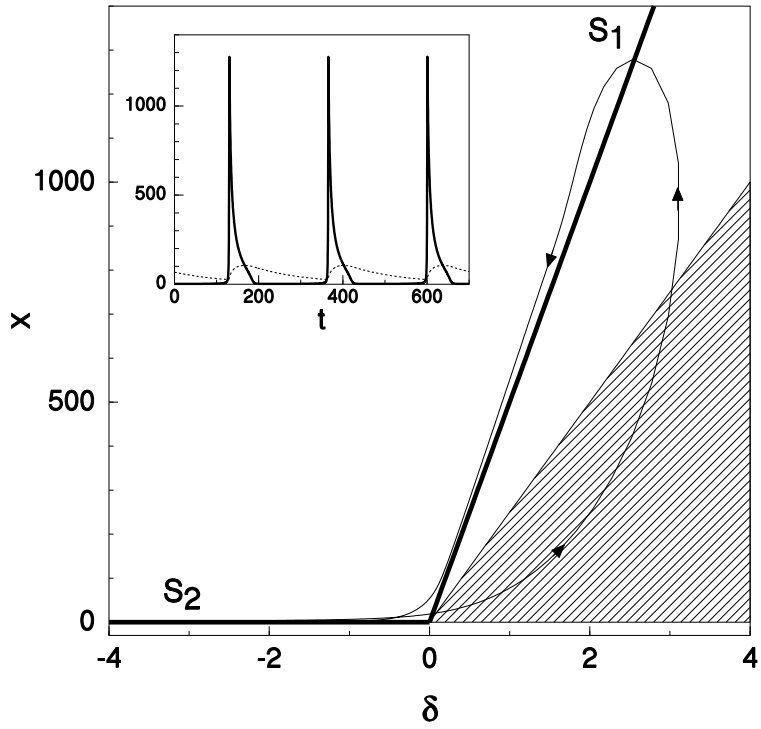

Fig. 6. Evolution of a trajectory (thin lines) along with the bent-slow manifold (S_1 and S_2 shown by thick lines) structure in the $x - \delta$ plane, for $m = 1.2$ and $e = 200$. Inset shows the time series of the x variable (continuous line) and z variable (dotted line).

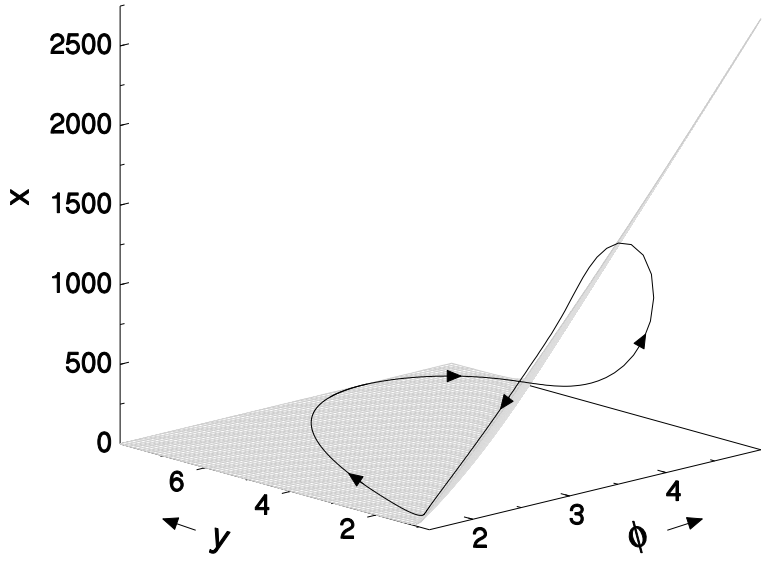

Fig. 7. Evolution of the trajectory along with bent-slow manifold (S_1 and S_2) structure in (x, y, ϕ) space indicated by the gray plane, for $m = 1.2$ and $e = 200.0$.

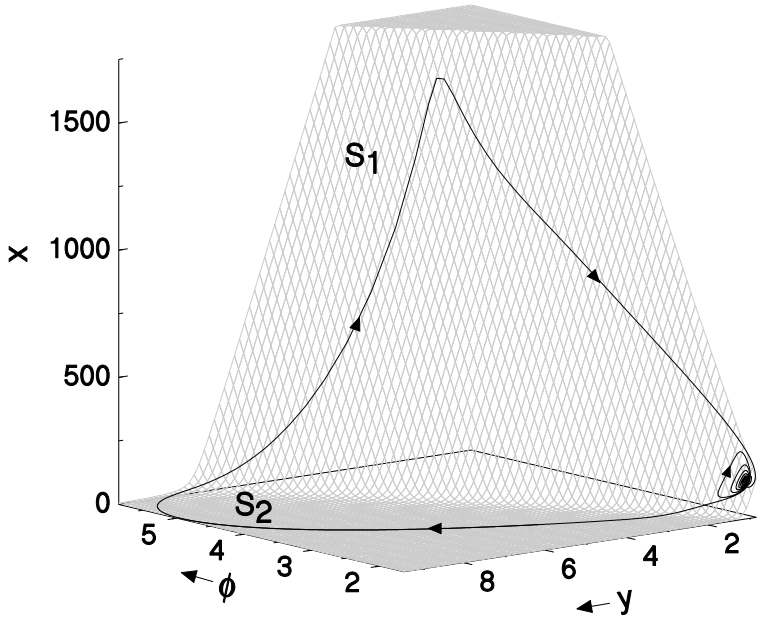

Fig. 8. Evolution of the trajectory along the bent-slow manifold (S_1 and S_2) structure for $m = 1.2$ and $e = 267.0$.

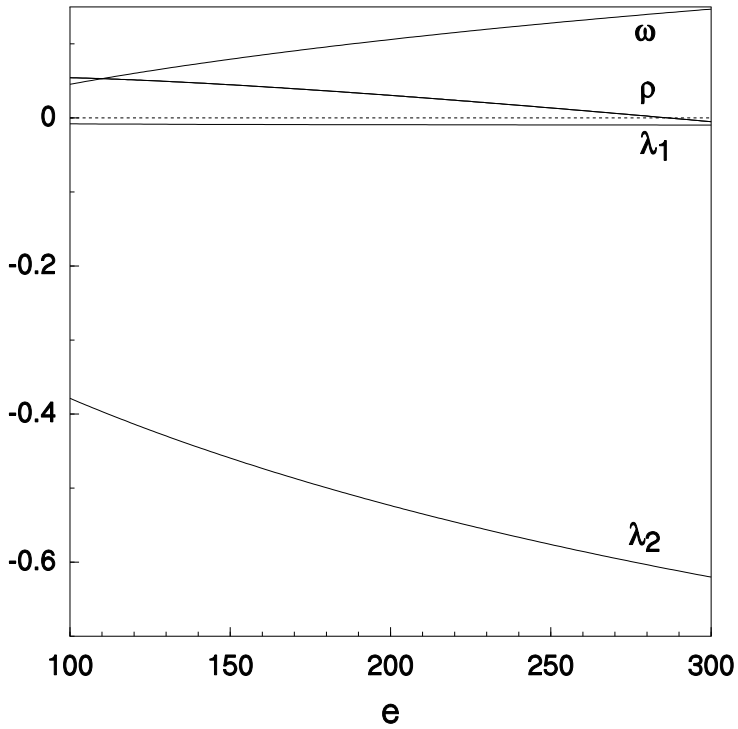

Fig. 9. Eigen value spectrum of the fixed point for $m = 1.2$. The dotted line represents the zero value.

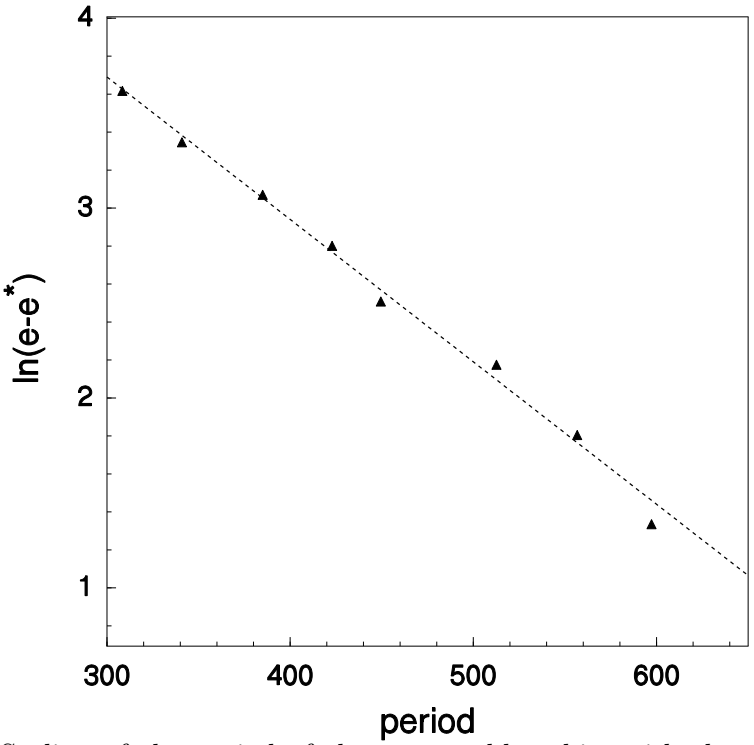

Fig. 10. Scaling of the period of the superstable orbits with the parameter for $m = 1.4$. The exponential scaling indicates the apparent approach to homoclinicity of the The exponential scaling indicates the apparent approach to homoclinicity of the saddle focus fixed point. Here e^* is taken to be the value of the twelve period orbit, $e = 247.63$.

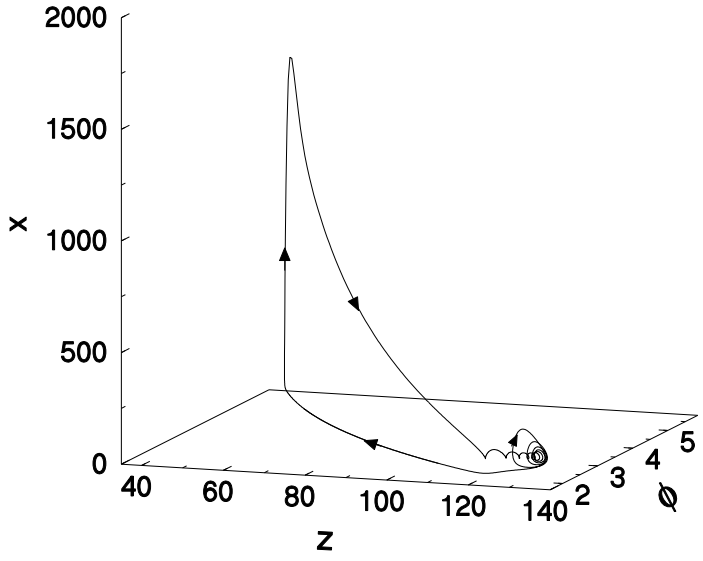

Fig. 11. Plot of a periodic orbit in (x, z, ϕ) space for $m = 1.2$ and $e = 267.0$ showing the eventual direction of approach towards the fixed point is z direction.

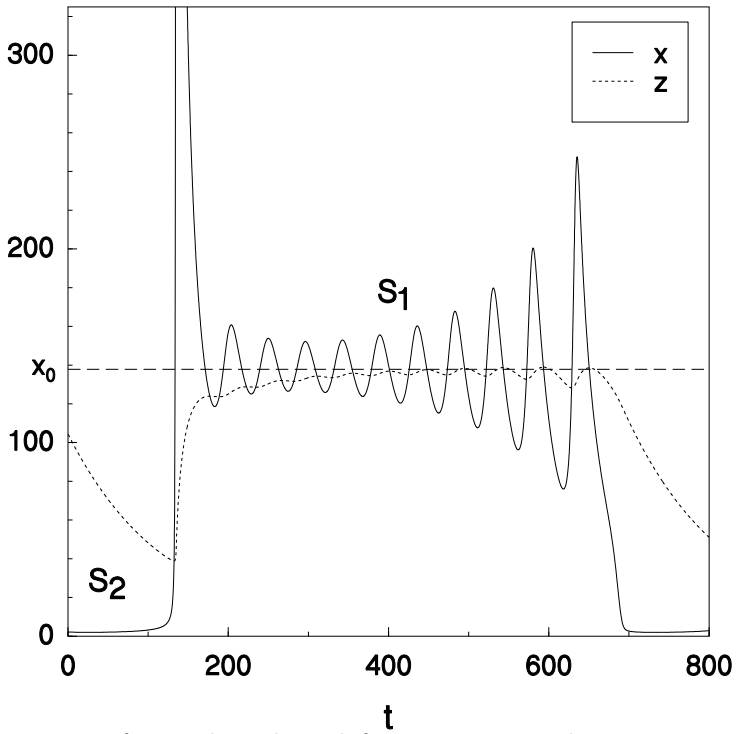

Fig. 12. Time series of x and z plotted for $m = 1.2$ and $e = 267.0$. Dashed line shows the fixed point value.

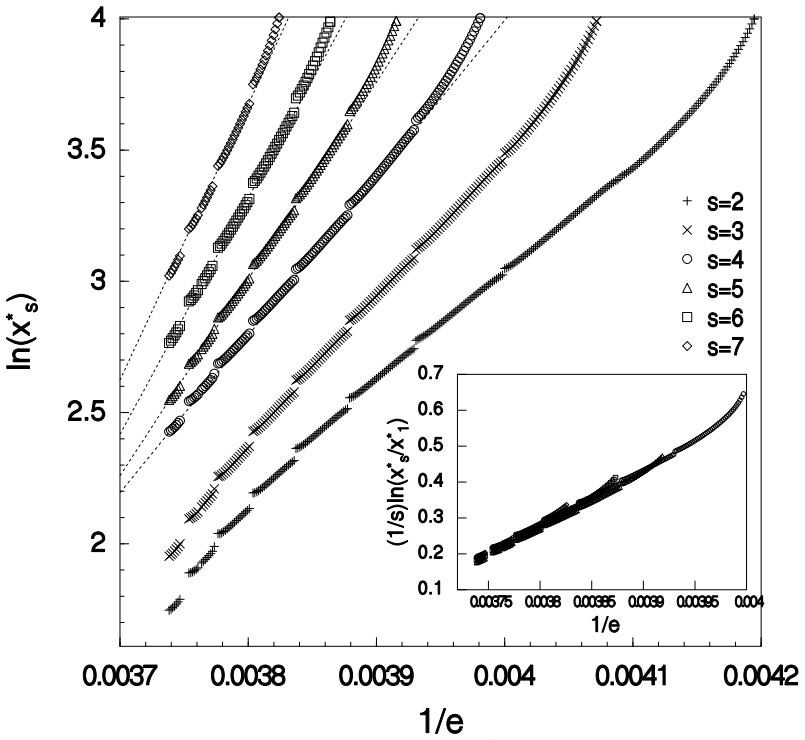

Fig. 13. Scaling of minimum value of x with e^{-1} for $n = 2, 3, \cdots, 7$ ($m = 1.2$). Inset shows collapse of all the curves from $n = 4$ to 7 onto a single curve. Dashed lines are shown as guide to the eye.

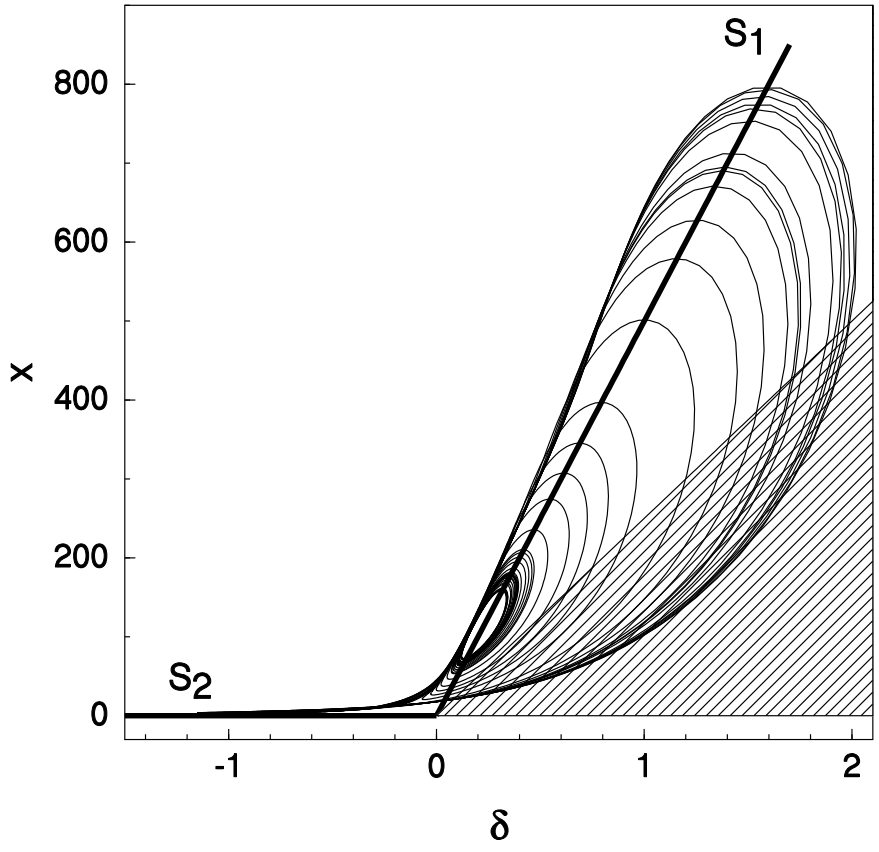

Fig. 14. A chaotic trajectory in $x - \delta$ plane for $m = 1.8$ and $e = 190.0$.